Monthly Notices of the ROYAL ASTRONOMICAL SOCIETY

MNRAS **544,** 53–66 (2025) https://doi.org/10.1093/mnras/staf1640
Advance Access publication 2025 September 26

A LOFAR search for coherent radio emission accompanying prompt engine activity in gamma-ray bursts

A. Hennessy [1★] R. L. C. Starling [1] A. Rowlinson [2,3] I. de Ruiter [2] A. J. van der Horst,[4] G. E. Anderson [5] N. R. Tanvir,[1] S. ter Veen,[3] K. Wiersema[6] and R. A. M. J. Wijers [2]

[1]*School of Physics and Astronomy, University of Leicester, University Road, Leicester LE1 7RH, UK*
[2]*Anton Pannekoek Institute for Astronomy, University of Amsterdam, Science Park 904, NL-1098 XH Amsterdam, the Netherlands*
[3]*ASTRON, the Netherlands Institute for Radio Astronomy, Oude Hoogeveensedijk 4, NL-7991 PD Dwingeloo, the Netherlands*
[4]*Department of Physics, George Washington University, 725 21st St NW, Washington, DC 20052, USA*
[5]*International Centre for Radio Astronomy Research, Curtin University, GPO Box U1987, Perth, WA 6845, Australia*
[6]*Centre for Astrophysics Research, University of Hertfordshire, Hatfield AL10 9AB, UK*

Accepted 2025 September 24. Received 2025 September 24; in original form 2025 January 14

ABSTRACT

Relativistic jets generated in gamma-ray bursts (GRBs) produce luminous transient events, yet the fundamentals of jet composition and radiation mechanisms remain unclear. One means of identifying a magnetically dominated outflow would be detection of prompt, coherent radio emission at low frequencies, and we are able to search for this using the LOw Frequency ARray (LOFAR) coupled with modelling of high-energy pulses detected by the *Neil Gehrels Swift Observatory* (*Swift*). We present the rapid response mode follow-up LOFAR observations of four long GRBs, each beginning within a few hundred seconds of the initial *Swift*-Burst Alert Telescope (BAT) trigger. We interpreted our findings under the framework of a magnetic wind model, predicting coherent radio emission analogous to prompt emission pulses. Using 60 and 180 s time-sliced imaging at 120–168 MHz, we obtain upper limits on radio pulse emission, finding no significant signals. In the case of GRB 200925B, we observed a small increase of radio flux seen at ∼60–360 s post-burst. In this model, this could represent the radio emission related to the *Swift*-BAT pulses, for a redshift of $z = 1.8$, however, with a low signal-to-noise ratio of ∼2, it is not deemed significant enough to confirm coincident prompt radio and gamma-ray emission. Instead, we can constrain the ϵ_B parameter, deriving upper limits of $\epsilon_B < 4.2 \times 10^{-4}$ for GRB 200925B. In GRB 240414A, with a reported redshift of $z = 1.833$, we constrain $\epsilon_B < 2.8 \times 10^{-4}$. We discuss these results in the context of our whole LOFAR rapid response sample of six long GRBs, finding our ϵ_B values are generally consistent with previous GRB studies.

Key words: gamma-ray burst: general – radio continuum: transients – X-rays: bursts.

1 INTRODUCTION

Gamma-ray bursts (GRBs) are the most energetic class of high-energy transients seen in the Universe, powered by a highly collimated relativistic jet. Since the first detection in 1967 (R. W. Klebesadel, I. B. Strong & R. A. Olson 1973), thousands of GRBs have been observed, yet many aspects of GRB physics remain poorly understood.

In this paper, we focus on the most commonly detected subset of GRBs known as long gamma-ray bursts (LGRBs), making up approximately 85 per cent (A. Lien et al. 2016) of bursts observed with the *Neil Gehrels Swift Observatory* (hereafter *Swift*; N. Gehrels et al. 2004). LGRBs occur during the deaths of a massive star in a core-collapse supernova. They typically occur with durations longer than ∼2 s (C. Kouveliotou et al. 1993), but this is detector dependent, and there is some overlap with the population of short gamma-ray bursts (SGRBs).

A GRB is characterized observationally by two key phases – the initial prompt high-energy emission generated within the relativistic jet, and longer lasting broad-band afterglow emission as the relativistic jet interacts with its environment. The prompt emission is observed as a number of highly energetic gamma-ray pulses on timescales of a few milliseconds to a few hundred seconds, likely caused by the interaction of internal energy shocks within the relativistic jet, resulting in the behaviour observed (R. Sari & T. Piran 1997). However, the nature of emission and the distance from the central engine which these shocks occur are still debated, in part due to the unknown composition of the jet. Additionally, a thermal component from the photosphere may be a significant contributor to emission in at least some bursts (A. Pe'er, P. Mészáros & M. J. Rees 2007; F. Ryde et al. 2010). A Poynting-flux-dominated jet can produce the prompt emission through a magnetic reconnection (e.g. V. V. Usov 1992). This works at higher efficiencies, but such models are highly dependent on magnetic field strength and configuration within the jet, which is not well known. M. J. Rees & P. Meszaros (1994) and D. Lazzati et al. (2013), for example, favour a matter-dominated jet, where collisions between shells at different Lorentz factors produce

★ E-mail: ah724@leicester.ac.uk

synchrotron radiation – one issue with this model is the relatively low efficiency of emission which is in tension with the energetics of the X-ray afterglow observations.

The subsequent afterglow displays temporal and spectral behaviour typical of synchrotron emission. X-ray afterglows are detected in the majority of GRBs (P. A. Evans et al. 2009), and afterglows are also seen at ultraviolet/optical through to radio wavelengths (e.g. D. A. Kann et al. 2011; G. E. Anderson et al. 2018). The detection of radio emission has proven a key diagnostic for the synchrotron-dominated afterglow physics (E. Waxman, S. R. Kulkarni & D. A. Frail 1998; P. Chandra & D. A. Frail 2012), and jet geometry, structure, and energetics (e.g. A. J. Horst et al. 2008; J. Granot & A. J. Horst 2014; L. Rhodes et al. 2024).

Radio signatures are also expected during the prompt emission phase for some magnetically dominated models. Magnetic reconnection is capable of releasing quick, powerful bursts that can reproduce the variability of GRB light curves (P. Beniamini & J. Granot 2016). At least one model predicts low-frequency radio emission to be emitted alongside the higher energy component through theoretical and simulation studies (M. V. Smolsky & V. V. Usov 2000; V. V. Usov & J. I. Katz 2000). In such models, the shock front of a relativistic, magnetized wind interacts with the ambient media, creating a surface current at the boundary. The strong electric field here accelerates electrons to relativistic speeds, causing X-ray and gamma-ray emission through synchrotron radiation. The interaction is highly variable, and the varying electric field induces low-frequency electromagnetic radiation.

This model potentially offers us a testable prediction for magnetically dominated GRB outflow: a radio flare analogous to gamma-ray pulses should be emitted, but observed later due to a dispersion delay (J. H. Taylor & J. M. Cordes 1993). As radiation travels through the host galaxy environment, intergalactic medium, and the Milky Way, longer wavelengths undergo greater dispersion, causing radio emission to arrive with a delay compared to the high-energy regime, typically on the order of a few hundred seconds at low radio frequencies. The brightness of the resultant radio flare depends on the energetics of the gamma-ray pulse, which are commonly modelled with fast rise and exponential decay (FRED) peaks (J. P. Norris et al. 1996) which can then be integrated across to calculate the total fluence.

The peak frequency of the emission in the magnetic wind models of V. V. Usov & J. I. Katz (2000) lies well below the capabilities of current radio facilities at ∼0.01 MHz, but telescopes like the LOw Frequency ARray (LOFAR; M. P. Haarlem et al. 2013), with receivers at 10–80 MHz and 120–240 MHz, and the Murchison Widefield Array (MWA; S. J. Tingay et al. 2013), operating at 80–300 MHz, should detect the higher frequency tail of this emission. R. L. C. Starling et al. (2020) provide a basis to show how LOFAR is capable of observing radio flares within this model, and establishing the mechanism for prompt GRB emission if found. This was done by demonstrating the detectability of predicted radio flares with LOFAR, given timing and flux density predictions calculated from a *Swift*-X-Ray Telescope (XRT) flare sample with the magnetic wind model applied. While the study leads us to expect a significant fraction of GRB X-ray flares would be detectable with the LOFAR High Band Antenna (HBA), a number of assumptions are folded into their calculations, and we re-examine these following the results of our study.

The MWA rapid-response mode (P. J. Hancock et al. 2019) is capable of repointing within 10 s of receiving a *Swift* GRB alert. Combined with dispersion delay, this makes MWA rapid enough to constrain prompt radio signals associated with the shocks within the jet (G. E. Anderson et al. 2021; J. Tian et al. 2022a) as well as X-ray flares (J. Tian et al. 2022b). Responsive modes have also been developed for the Long Wavelength Array at Owens Valley Radio Observatory to capture fast radio transients associated with GRBs and gravitational waves (N. Kosogorov et al. 2025). While LOFAR's current response time of ∼4–5 min means it will not catch the very first radio pulses from a GRB, its superior sensitivity allows us to deeply probe radio pulses associated with X-ray flares (A. Hennessy et al. 2023) and other prompt radio emission mechanisms (A. Rowlinson et al. 2019, 2021, 2024).

One of the more uncertain parameters is the fraction of total energy in the magnetic field in the GRB jet, ϵ_B. This has direct consequences on interactions within the jet, and importantly, it controls the brightness of radio emission in the magnetic wind model. The dynamic nature of the event and surroundings means this parameter should evolve over the lifetime of the burst (A. K. Ror et al. 2024) and is likely somewhat variable across different bursts. Several studies obtain ϵ_B value estimations through GRB afterglows (e.g. R. Barniol Duran 2014; P. Beniamini et al. 2015; J. K. Leung et al. 2021), finding a wide range of values and upper limits spanning many orders of magnitude. However, the dynamic evolution of the jet, and hence also the magnetic field of the jet, means that ϵ_B may not be directly comparable between the prompt, as studied in this paper, and afterglow phases.

Especially during the prompt emission phase, the transient nature of GRBs can make detection and follow-up inconsistent. Each burst is unique temporally and spectrally, and while many show common features, no model has been successful in explaining all observations; see P. Kumar & B. Zhang (2015) for a comprehensive review. Prompt emission coverage has been challenging at low frequencies; however, two LGRBs have already been investigated through a rapid response follow-up with LOFAR (A. Rowlinson et al. 2019; A. Hennessy et al. 2023) and a further one through follow-up with MWA (J. Tian et al. 2022b). All of these early-time studies draw similar conclusions: no coherent radio emission is detected, allowing for constraints to be placed on the parameters within the magnetic reconnection model of V. V. Usov & J. I. Katz (2000) – in particular ϵ_B, estimating upper limits of $\sim 10^{-4}$.

This only represents a total of three attempts at observing prompt radio emission from a LGRB. Especially given the uncertain properties of the relativistic jets and the surrounding medium in each burst, this is not sufficient to begin to test whether the emission was simply not bright enough to observe with current facilities, if some (or all) pulses are obscured by the local environment, or whether these pulses simply do not occur. LGRB durations are highly variable, and together with the broad redshift distribution, this means the timing of the radio observations is important. Yet, the triggered radio observations are all performed identically, and no LGRB rapidly observed at low frequencies thus far has had a secure redshift at the time of trigger. The dispersion measure (DM) through differing sightlines through the Milky Way, and especially the host galaxy, will be different for each burst and a more complete study can be beneficial for understanding this better. This method has the potential to probe GRB jet composition, shock locations, and environments, given a sufficiently large set of observations, such that the parameters going into the modelling can be disentangled.

In this paper, we present an analysis of LOFAR HBA data of a further four LGRBs, more than doubling the total number of LGRBs followed up: GRB 200925B, GRB 210104A, GRB 240414A, and GRB 240418A, all bursts observed as part of a rapid response

campaign. GRB 210104A and GRB 240414A include reported redshifts as part of other follow-up.

In Section 2, we detail the *Swift* and LOFAR observations for each burst. Section 3 describes the methods used to analyse and present the data. In Section 4, we describe the magnetic wind model that predicts coherent radio emission to be emitted analogous to gamma-ray pulses. Section 5 presents the light curves and results of the collected data in the context of the magnetic wind model – we discuss how we can constrain parameters due to non-significant detections of radio emission, and in one case, assuming a low-significance bump may be a real radio flare, and the limitations leading to non-observable radio flares. We discuss all the LGRBs from the LOFAR campaign as a whole in Section 6.1 alongside estimates of ϵ_B in other literature. Finally, we conclude in Section 7.

2 TARGETS

Here, we summarize the key information for the four LGRBs presented in this work. The burst durations are defined by the T90, the time period for 5–95 per cent of photons from the prompt phase to be detected.

2.1 GRB 200925B

GRB 200925B triggered the *Swift* Observatory on the 2020 September 25 at 21:50:37 UT. The T90 in the 15–350 keV range is reported as 18.25 ± 0.97 s, designating this burst as an LGRB (M. Stamatikos et al. 2020). The Burst Alert Telescope (BAT; S. D. Barthelmy et al. 2005) was triggered by this burst and detected for ∼40 s. Simultaneously, the spacecraft was slewed and the XRT instrument (D. N. Burrows et al. 2005) onboard began collecting data 78.4 s after the initial trigger (B. Sbarufatti et al. 2020).

No redshift was obtained for this burst. An optical afterglow was found in the *I* band (A. Ugarte Postigo et al. 2020), placing an upper limit of $z \lesssim 5.5$.

LOFAR's rapid response mode was automatically triggered, and with the GRB position being immediately observable, LOFAR HBA began observing the target location at 21:55:04 UT, 267 s after the initial BAT trigger, collecting 2 h of imaging data.

2.2 GRB 210104A

Swift-BAT was triggered at 11:26:59 UT on 2021 January 4, collecting ∼40 s of gamma-ray data. The prompt emission shows a highly variable structure with a number of distinctive peaks. The reported T90 is 32.06 ± 0.49 s (D. M. Palmer et al. 2021). *Swift*-XRT began observations 69 s after the initial trigger (J. A. Kennea et al. 2021).

LOFAR automatically triggered at 11:31:28 UT and began collecting 2 h of imaging data, 269 s after the BAT trigger.

For this burst, there is a tentative redshift of $z = 0.46$ reported through spectroscopic observations of absorption features (L.-L. Zhang et al. 2022).

2.3 GRB 240414A

GRB 240414A occurred at 02:20:36 UT on the 2024 April 14 after triggering *Swift*-BAT. The prompt emissions show a similar structure to that of GRB 200925B, characterized by several pulses, and a final short pulse during the rapid decay phase before giving way to afterglow emissions. The T90 as reported by BAT was 88.28 ± 50.41 s (C. B. Markwardt et al. 2024). BAT collected about 300 s of data, and the spacecraft slewed and an XRT position was promptly available, but XRT data are only available from 10 000 s (S. Dichiara et al. 2024).

A redshift of $z = 1.833$ is reported for this burst as the result of optical observations of a number of absorption features (C. Adami et al. 2024; A. Ugarte Postigo et al. 2024), observed by the MISTRAL (Multi-purpose InSTRument for Astronomy at Low-resolution; J. Schmitt et al. 2024) and GTC/OSIRIS+ (Gran Telescopio Canarias/Optical System for Imaging and low Resolution Integrated Spectroscopy; J. Cepa 1998).

LOFAR triggered at 02:26:49 UT and began collecting 2 h of follow-up imaging data, 373 s after the initial BAT trigger.

2.4 GRB 240418A

Swift-BAT triggered on the 2024 April 18 at 20:24:08 UT with a reported T90 of 12.00 ± 3.61 s (D. M. Palmer et al. 2024). *Swift*-XRT began observing 122 s after the BAT trigger, revealing a featureless, decaying afterglow in 6.1 ks of X-ray data (A. Tohuvavohu et al. 2024). Several optical facilities were unable to detect an optical counterpart with limiting magnitudes of $r > 22$, $z > 20.4$, and $J > 19$, but NIRES (Near-Infrared Echellette Spectrograph) identified an afterglow candidate in the *K'* filter with magnitude 20.9 ± 0.1 (V. Karambelkar et al. 2024).

Imaging with LOFAR's rapid response mode was triggered 373 s after the initial trigger at 20:30:21 UT.

3 METHODS

Here, we detail the methods used to present and analyse the gamma-ray, X-ray, and radio data.

3.1 *Swift* data

In order to produce predictions for the flux density of radio flares emitted analogous to prompt emission pulses, described later in Section 4, the light curves and flares need to be modelled to calculate the fluence from each flare component.

We obtained the flux density data for BAT and XRT (at 50 and 1 keV, respectively) from the online *Swift* archive[1] at the UK *Swift* Science Data Centre (UKSSDC; see P. A. Evans et al. 2007, 2009). XRT data use all available observation modes where provided. The combined light curves for each burst are displayed in Fig. 1.

Selected light curves are fitted with our code that models the flares and afterglows of GRBs, described in A. Hennessy et al. (2023). To summarize, the code first identifies flares by requiring that at least two out of three consecutive data points rise at least twice the first point's 90 per cent confidence interval. Start, peak, and end times are found through local minima, maxima, and by calculating the changing gradient, and excluded. The remaining data represent the afterglow and are fitted with a broken power-law model of up to five breaks. Finally, the flares are modelled as FRED peaks, described by

$$f(t) = A \times \sqrt{\exp\left(2 \times \frac{R}{D}\right)} \times \exp\left(-\frac{R}{t - t_s} - \frac{t - t_s}{D}\right), \quad (1)$$

where A corresponds to amplitude, R and D are variables determining the rise and decay steepness, and t_s is the start time of the modelled flare. FRED flares represent a fast energy release followed by some

[1] https://www.swift.ac.uk

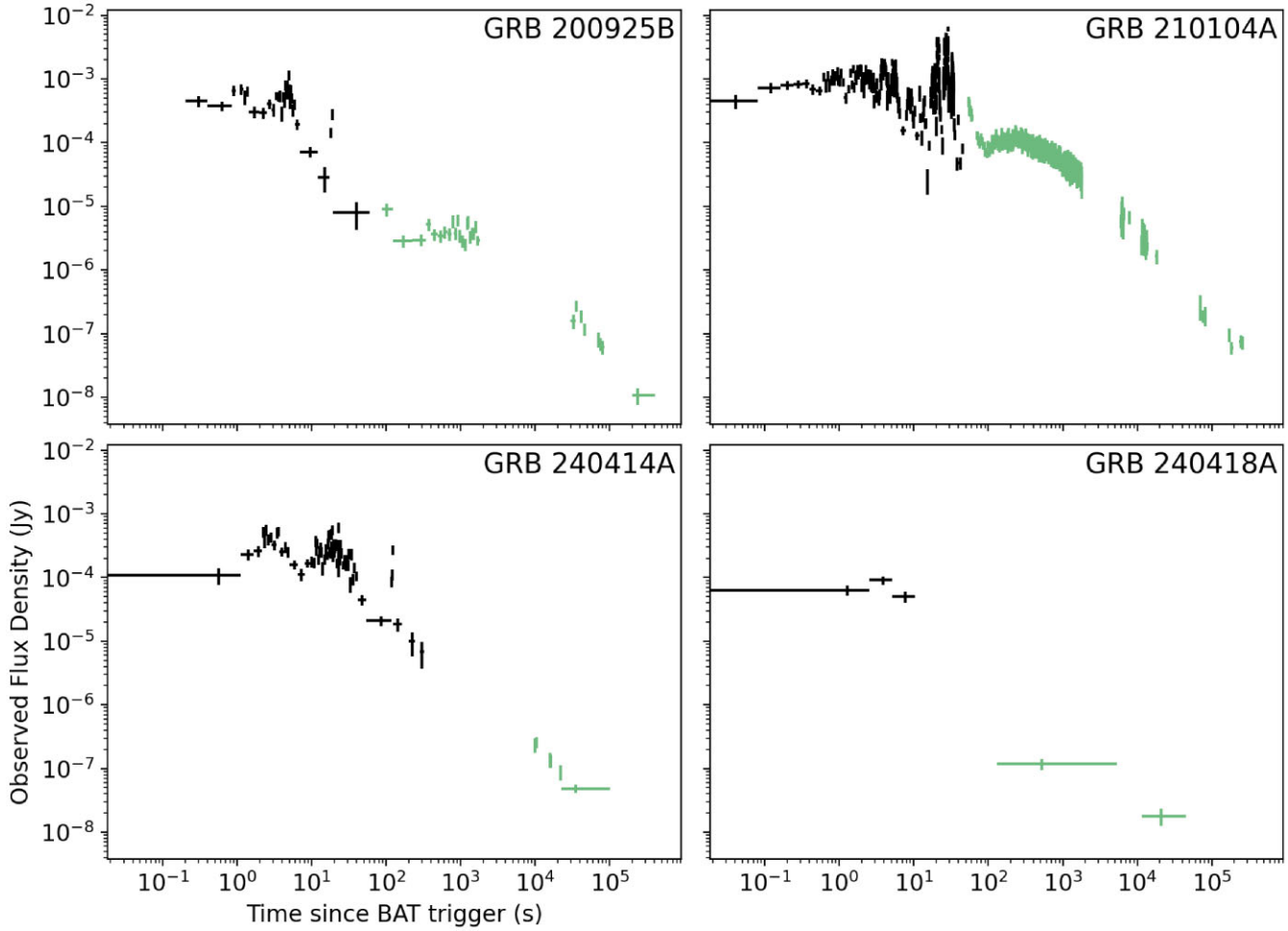

Figure 1. The observed flux density light curve for early *Swift*-BAT (at 50 keV) and later *Swift*-XRT (at 1 keV) for the four GRBs presented in this paper.

slower diffusive process and are associated with several transient phenomena, specifically, they model well the prompt emission pulses in many GRBs (J. P. Norris et al. 1996; G.-L. Ma et al. 2024).

Since the data collected are in units of observed flux density in this case, to fit BAT and XRT data simultaneously, we must convert to units of flux in each instruments' native frequency in order to integrate and measure a fluence. Spectral evolution data from the power-law fits to the spectra are made available from the *Swift* Burst Analyser (P. A. Evans et al. 2010), allowing us to convert from flux density at 50 keV to flux in the 15–50 keV energy range for the BAT data. The flares we are modelling are only present in the BAT data for this study, but we model and plot the *Swift*-XRT for completeness – available from the *Swift* light-curve repository (P. A. Evans et al. 2007, 2009).

3.2 LOFAR data

LOFAR rapid response observations were initiated automatically using a custom-built script to parse *Swift* GCN Notices (using VOEVENT-PARSE tools; T. D. Staley 2014),[2] select appropriate GRBs, and communicate with LOFAR. Trigger criteria demanded that the GRB be observable to LOFAR within 10 min of the *Swift*-BAT trigger at an elevation of $\geq 20^{\circ}$ for at least 30 min, with an optimal calibrator source simultaneously available. We also required a BAT rate trigger significance of $\geq 10\sigma$ (the photon count rate significance over background noise) or rate trigger integration time-scale of ≤ 2 s (the event duration likely represents an SGRB), and a prompt *Swift*-S/C Will_Slew notice[3] to ensure XRT observations and hence a refined localization on the order of arcseconds.

All observations were made in the 120–168 MHz frequency range using the LOFAR HBA. The data were averaged with a 1 s integration time in 244 sub-bands of 195.3 kHz. The Dutch array was used, composed of 23 core stations and 11 remote stations, yielding a maximum baseline of 121 km (M. P. Haarlem et al. 2013). After the target observations, a 10 min calibration observation was taken.

The data were averaged to 8 s time resolution then calibrated and imaged using the LOFAR Initial Calibration (LINC, version 4.0) pipeline,[4] used to correct for instrumental effects in LOFAR observations. Standard software and methods were used, as described in R. J. Weeren et al. (2016), W. L. Williams et al. (2016), and F. Gasperin et al. (2019). Part of the process includes AOFLAGGER, version 3.3 (A. R. Offringa et al. 2010; A. R. Offringa, J. J. van de Gronde & J. B. T. M. Roerdink 2012), to allow statistical flagging and removal of data affected by radio interference. We used a

[2] https://voevent-parse.readthedocs.io/en/stable/

[3] A GCN notice that *Swift* will slew to the GRB position and continue to observe the target.

[4] https://linc.readthedocs.io/en/latest/

Table 1. A summary of the LOFAR observations.

GRB	Project code	Observation ID	Calibrator	Start time	Duration (s)
200925B	LC14_004	796116	3C 295	21:55:04	7199
210104A	LC15_013	815080	3C 147	11:31:28	7199
240414A	LC20_021	2039208	3C 295	02:26:49	7200
240418A	LC20_021	2039344	3C 286	20:30:21	7200

calibrator observation (see Table 1) to derive gain solutions, which are transferred to the target observation. A phase-only calibration was applied to the target data using a sky model from TGSS ADR1 (TIFR GMRT Sky Survey Alternative Data Release 1)[5] (H. T. Intema et al. 2017). We decided that further direction-dependent calibration was not required in any case, as the GRBs were at the centre of the field in each observation.

The calibrated files were imaged with WSCLEAN (version 3.1.1; A. R. Offringa et al. 2014),[6] a wide-field interferometric imager. Standard imaging parameters were used: Briggs weight −0.5 and autothresholding to 100 000 iterations. A pixel scale of 1 arcsec was used with a 2048 × 2048 pixels image size.

A deep image was created for each LOFAR observation, showing the GRB and surrounding region, shown in Fig. 2, to look for any persistent emission at the GRB position, such as from the host galaxy. Time-sliced images using the full frequency range were also created to produce radio light curves, at 60 and 180 s intervals, using the same imaging parameters. These time lengths were selected based on a dispersed flare length of ∼300–400 s (R. L. C. Starling et al. 2020; A. Hennessy et al. 2023). A choice of bin width equal to the radio flare width would result in only one elevated point per flare, which would hamper positive identification, while choosing a width much less than half the flare width runs the risk of low signal-to-noise ratio per bin also hampering identification. Consequently, a 60 s time slice may allow us to observe the rise and fall structure of a radio flare.

The LOFAR Transients Pipeline (TRAP, version 6.0; J. D. Swinbank et al. 2015)[7] is a pipeline that looks for transient or variable sources within astronomical data, primarily designed for LOFAR data. We used TRAP to obtain flux measurements in each image using a force fit extraction at the GRB position. TRAP also outputs a background root mean square (rms) noise in each image, calculated using the inner 1/8th of the image. For time-sliced images, source extraction is undertaken for each slice using default settings and restoring beam, allowing us to create a radio light curve at the location of the GRB.

Where there was a flux density enhancement found, we created images across six frequency channels using the 60 s interval data to create individual light curves at each channel frequency, as a means of looking for a dispersed signal.

4 MAGNETIC WIND MODEL

The V. V. Usov & J. I. Katz (2000) model describes a relativistic, strongly magnetized wind that interacts with the negligibly magnetized intermediate media surrounding the burst, creating a surface current at this boundary with a very strong electric field. This accelerates electrons in the plasma to relativistic speeds, resulting in the synchrotron spectrum observed at X-ray and gamma-ray wavelengths. Additionally, the model also predicts low-frequency electromagnetic waves to be produced at the same time due to a varying electric field from the non-stationarity of the interaction. We should expect to see radio emission emitted during the prompt emission phase similar to how we see pulses in gamma-rays.

R. L. C. Starling et al. (2020) applied this model to existing data, predicting that 44 per cent of X-ray flares in a sample of *Swift* GRBs with redshifts should have a detectable prompt radio component at 144 MHz with LOFAR HBA, assuming that X-ray flares arise from the same internal mechanisms as gamma-ray pulses. We follow the method of a previous analysis of a single GRB studied through this LOFAR follow-up campaign, described in A. Hennessy et al. (2023).

The emissions from the source are dispersed due to the interactions with intermediate matter along the line of sight to the GRB, and hence the radio emission is delayed relative to the gamma-rays. This delay $\tau(\nu)$ is estimated as

$$\tau(\nu) \sim \frac{\mathrm{DM}}{241\nu^2}\ \mathrm{s}, \tag{2}$$

where DM is the dispersion measure (units of pc cm^{-3}) and ν the observing frequency in GHz (J. H. Taylor & J. M. Cordes 1993).

DM is expected to scale with the number of free electrons along the line of sight. Therefore, a larger DM is expected for sources at a larger distance, or for sources with particularly dense host environments. In this paper, we follow D. R. Lorimer et al. (2007) and other similar LOFAR rapid response studies of GRBs and take DM as $\sim 1200z$ pc cm^{-3} (A. Rowlinson et al. 2019; A. Hennessy et al. 2023).

The predicted flux density for a radio pulse, in the dispersion limited case, based on the fluence in gamma-ray pulses is given (by V. V. Usov & J. I. Katz 2000) as

$$F_\nu = \frac{\delta(\beta-1)}{2\Delta\nu\tau(\nu)}\left(\frac{\nu}{\nu_{\max}}\right)^{1-\beta}\frac{\Phi_\gamma}{10^{-23}}\ \mathrm{Jy}, \tag{3}$$

where $\delta \sim 0.1\epsilon_B$ is the ratio of bolometric radio fluence (120–168 MHz) to bolometric gamma-ray fluence (15–50 keV), β is the spectrum power-law index in the high-frequency radio tail ($\gtrsim$0.01 MHz), $\Delta\nu$ is the observing bandwidth (48 MHz), $\nu_{\max}$ is the peak frequency of radio emission (see equation 1 in A. Hennessy et al. 2023), and Φ_γ is the bolometric gamma-ray fluence in erg cm^{-2}. The emission occurs over a range of frequencies, and hence will experience broadening due to the effects of dispersion delay varying based on frequency. The form of equation (3) accounts for this broadening in the dispersion limited regime. For all flares in this study, we are in this regime, where the dispersion broadening dominates over the intrinsic flare length, in this case assumed to be the same length as the gamma-ray pulse.

As a result, we are able to analyse the LOFAR radio data sets and test predictions of this model for bursts with prompt gamma-ray pulses for which the redshift is known.

[5]Tata Institute of Fundamental Research Giant Metrewave Radio Telescope Alternative Data Release.
[6]https://wsclean.readthedocs.io/en/latest/
[7]https://docs.transientskp.org

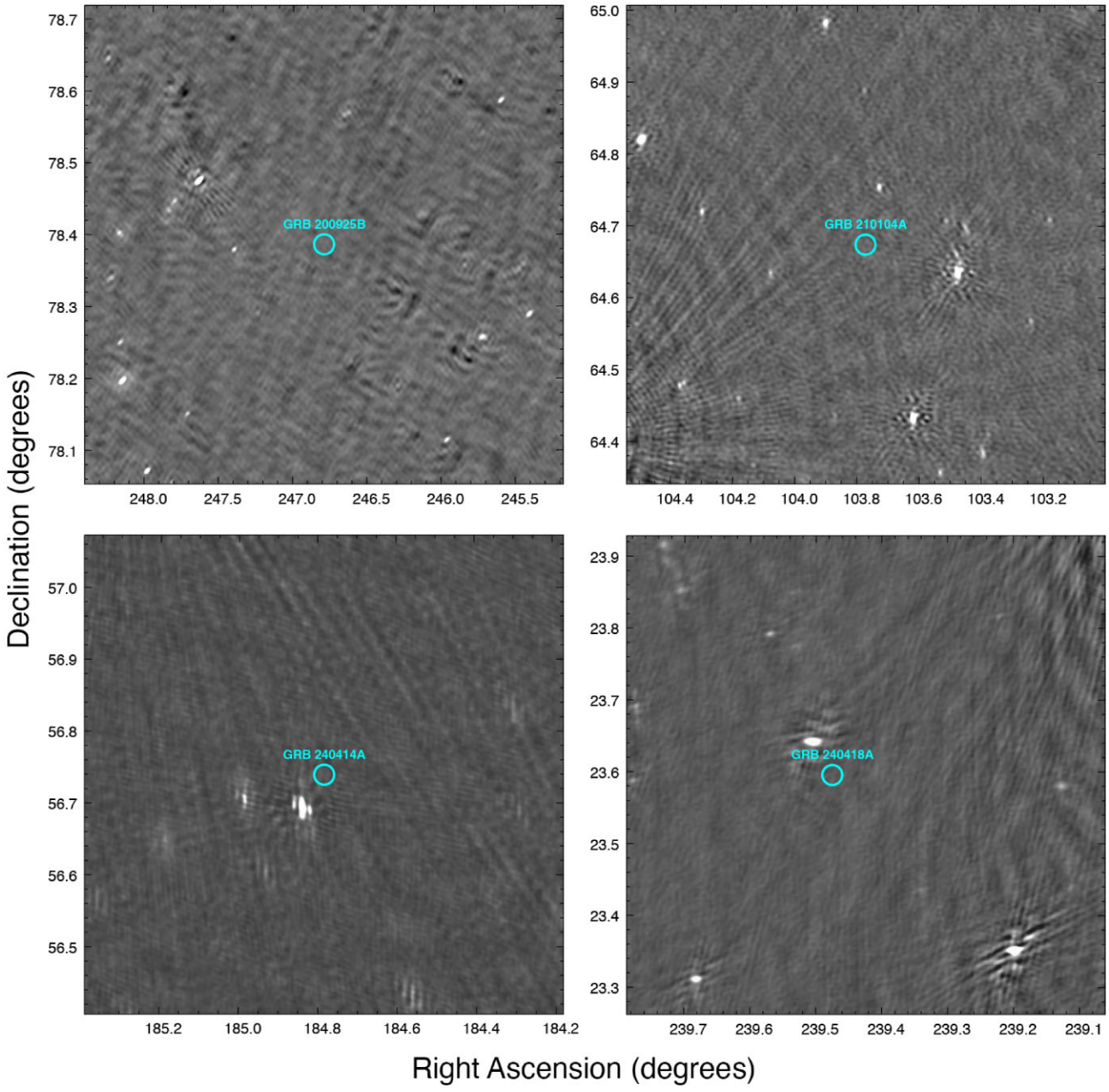

Figure 2. The deep LOFAR images spanning the full 2 h of available data for each GRB data set. From top-left clockwise: GRB 200925B, GRB 210104A, GRB 240418A, and GRB 240414A. All images are 40 × 40 arcmin^2. The circles are the position of the GRB, the size of the circles is 50 arcsec and are only meant to guide the eye.

5 RESULTS OF THE SEARCH FOR COHERENT RADIO EMISSION

5.1 GRB 200925B

The results for GRB 200925B are shown in Fig. 3, where we fit the BAT–XRT light curve and present the 144 MHz radio flux light curves. The high-energy light curve is well modelled with three breaks in the continuum, showing a fairly standard 'canonical' GRB, as described in P. A. Evans et al. (2009); and two flares seen in the BAT data during and just after the prompt emission phase, peaking at 4.9 and 19.1 s. The measured 15–50 keV fluences for the two flares are 6.33×10^{-8} and 1.51×10^{-7} erg cm^{-2}, respectively. See Table 2 for a summary of the modelled flares.

In both 60 and 180 s binned light curves, we observe no significant radio emission. We note a small 2σ (twice the rms) bump in both light curves at ∼120 s, seen in one 120 s image and five consecutive 60 s images. We searched for a dispersed signal over the time of this bump by looking at each frequency channel individually. Consecutively delayed peaks are expected, with the lower frequencies arriving later, due to dispersion.

We expect the two flares seen in the high-energy regime to produce a corresponding signal at radio frequencies in line with the model discussed in Section 4. We require a minimum value of $z \gtrsim 1.05$,

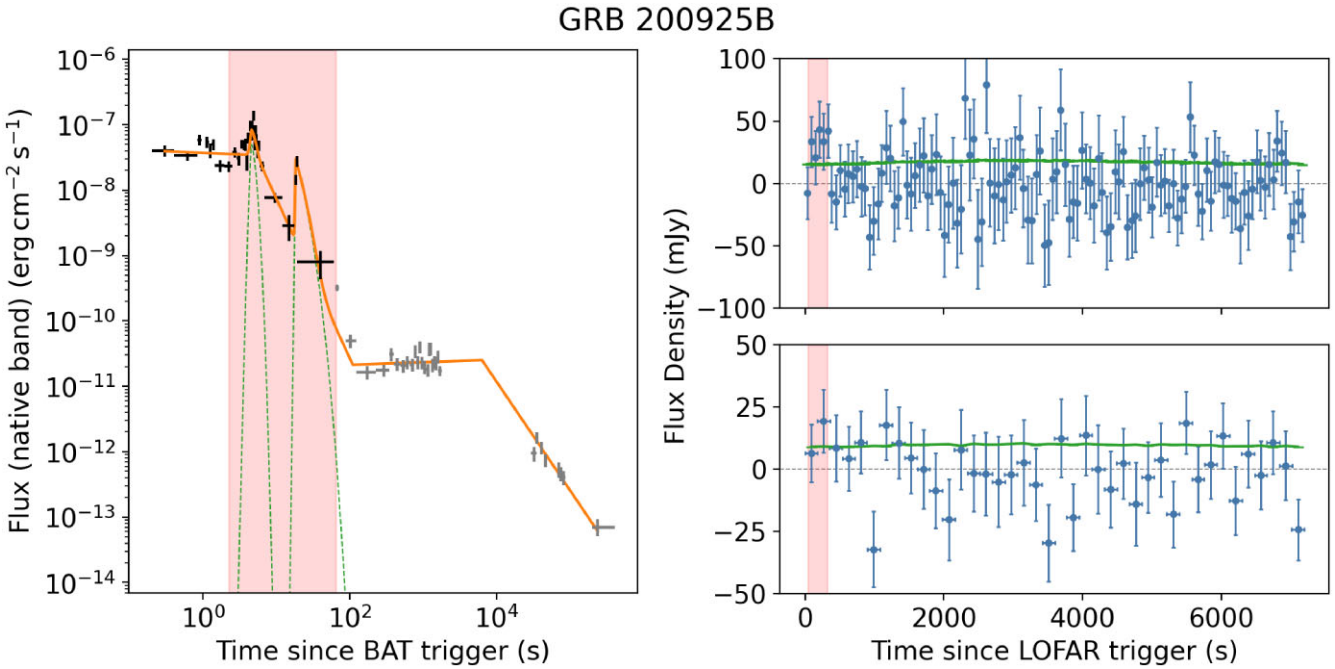

Figure 3. Left: The flux light curve of GRB 200925B for earlier BAT data (15–50 keV) and later XRT data (0.3–10 keV). Overlaid is the result of the GRB modelling curve described in Section 5 (and in further details in A. Hennessy et al. 2023) – flare (dashed line) components are shown, and the total model fit (solid line) is shown. Table 2 contains a summary of the fit. Three power-law breaks and two flares are found for this burst. Right: The observed 144 MHz radio flux density at the position of GRB 200925B as a function of time. The top panel shows the 60 s time-sliced images, and the bottom panel shows the 180 s time-sliced images. The rms noise in each image is shown by the solid line. The shaded region across all panels shows the predicted timing and duration of a radio flare overlapping a 2σ bump, which corresponds to the red-shaded region in the *Swift* light curve, for $z \sim 1.8$.

Table 2. Summary of the light curves fitted with our code for the two GRBs with a redshift (Figs 3 and 5). The afterglow is fitted with a broken power law, and the flares fitted with a FRED curve (equation 1).

GRB	Flare #	Temporal index under flare	Flare parameters[a]			Flare start/peak/end (s)			Flare γ-ray fluence (15–50 kev) (erg cm^{-2})
			t_s	R	D				
200925B	1	0.05	3.42	8.53	0.19	2.24	4.94	6.34	6.33×10^{-8}
	2	2.44	18.16	0.002	5.13	14.80	19.06	64.99	1.51×10^{-7}
240414A	1	0.05	−1.17	25.53	0.60	0.56	2.46	7.30	9.63×10^{-8}
	2	0.05	−0.41	113.26	2.66	7.30	22.92	30.24	4.00×10^{-7}
	3	1.42	111.93	92.36	3.00	85.48	122.10	222.28	5.15×10^{-7}

[a] As described in Section 3.1.

resulting in a dispersion delay of 252 s, for both analogous radio peaks to be sufficiently delayed into the LOFAR observation window, given the 267 s delay for observations to start compared to the BAT trigger. Alternatively, $z \gtrsim 1.10$ produces conditions for just the latter, more energetic peak to become observable in the data, with a dispersion delay of 265 s in this case. However, $z = 1.8$ produces a dispersion delay of 428 s which is sufficient for the predicted timing of the flare to fall at the time of the small bump seen in one 180 s and several consecutive 60 s bins. Looking at the timing of arrival of maximum flux in each frequency channel, a dispersed signal is not evidenced.

The observed pulse width will be longer than the intrinsic pulse width as a result of dispersion – the pulse occupies a finite frequency range, where each part is dispersed by a slightly different amount. By modelling the temporal shape of the intrinsic pulse as a delta function, we estimate the observed duration as 285.4 s at $z = 1.8$ (equation 3, A. Hennessy et al. 2023). The real pulse will have some finite length, so we expect this to offer a lower limit on the total duration of observed radio emission, but expect the peak emission to occur in this time frame. Given the width and separation of the two gamma-ray pulses seen in the *Swift* light curve (Table 2), we expect the radio pulses to be almost totally overlapping.

Assuming a non-detection of radio emission in these images, we obtain an output rms value of 17.1 and 9.6 mJy to derive a 3σ ($3\times$ rms) upper limit on any flaring activity of 51.3 and 28.8 mJy, for integration lengths of 60 and 180 s, respectively.

Subsequently, in Section 5.5, we discuss the implications of a non-detection on the input parameters of our model. We also consider the case and implications of a radio signal being observed, in line with the observed, low-significance bump in the radio light curve.

5.2 GRB 210104A

The high-energy afterglow modelling finds four power-law breaks and 16 flares in the energetic prompt phase. However, these flares are not accessible due to the combination of the reported redshift of $z = 0.46$ producing a dispersion delay of 110.5 s and LOFAR's 269 s

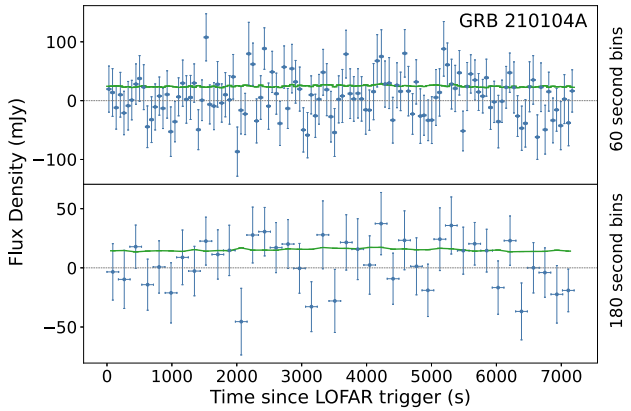

Figure 4. The observed 144 MHz flux density at the position of GRB 210104A as a function of time, for 60 and 180 s time slices. The solid line shows the 1σ rms noise measured in each image.

response time – in this case the predicted timing of the radio flares would be before observations began. Our LOFAR observation begins only during the plateau phase of the afterglow. We note, however, there is a possibility the redshift is higher, up to a limit of about $z = 2.2$, due to no significant host being found and based on the lack of a clear Ly α line in the optical spectrum.

The 144 MHz radio flux light curve is shown in Fig. 4. In both 60 and 180 s binned images, we do not detect any significant radio signal for this burst, and we obtain an output rms value of 24.5 and 15.1 mJy to derive 3σ upper limits of 73.5 and 45.3 mJy, for integration lengths of 60 and 180 s, respectively.

5.3 GRB 240414A

GRB 240414A is found to have one power-law break and three flares, in the high-energy data when fitted with our light-curve modelling code. The prompt phase shows several energetic pulses. The flares peak at 2.46, 22.92, and 122.10 s with integrated 15–50 keV fluences of 9.63×10^{-8}, 4.00×10^{-7}, and 5.15×10^{-7} erg cm^{-2}, respectively. The final few BAT data points may indicate the existence of another flare, but there is insufficient data to attempt to model this.

The reported redshift $z = 1.833$ produces a dispersion delay of ∼440 s. LOFAR's response time of 373 s means that we should expect to see the equivalent radio emission in the first few bins of our radio light curve – though the TRAP source extractor is unable to produce a data point for some time slices due a large percentage of the data being flagged, representing poor-quality data, usually due to interference from atmospheric conditions.

The fit of the *Swift*-BAT and XRT light-curve data and radio light curve are displayed in Table 2 and Fig. 5. In 60 and 180 s binned sets of images, we observe no significant radio emission. The quality of some parts of this observation was lower, leading to heightened flagging in the LINC pipeline. The first 180 s (and first three 60 s) bins were unable to be imaged, cutting off some data during the predicted radio timing. We should still expect to see most of the emission from the latest, most energetic flare. For a higher fraction of energy in the magnetic field, $\epsilon_B = 10^{-3}$, the radio flux density is predicted to be 281 mJy just for the third flare, which is not observed. However, a more conservative estimate of $\epsilon_B = 10^{-4}$ predicts 14 mJy, in which case the emission would be obscured in the noise, consistent with our findings.

Regardless of the true ϵ_B value, we can place an upper limit on any radio emission at this time – an image rms of 30.7 mJy produces a 3σ limit of 92.2 mJy for 60 s bins, and a rms of 21.8 mJy produces a 3σ limit of 65.4 mJy on any 180 s emission.

5.4 GRB 240418A

The *Swift* BAT–XRT data for this burst showed very little structure, and there is no reported redshift, meaning we are unable to directly test the magnetic model with this data set. In this case, the data quality was not sufficient to image on 60 s time-scales.

We have nevertheless imaged the data anyway to test for any radio emission and shown this in Fig. 6. We report no significant emission in our images, but are able to derive a 3σ upper limit of 79.5 mJy for an integrated length of 60 s.

5.5 Low significance enhancement in GRB 200925B

In GRB 200925B, we note a $\sim 2\sigma$ increase in flux density at a time that would be analogous to the gamma-ray pulses emitted in the prompt emission for $z = 1.8$. The predicted duration of each flare at this redshift is ∼258 s. The proximity of the flares in the *Swift*-BAT data means we should expect the radio flares to be observed overlapping and hence expect a slightly longer duration, and a summed 144 MHz flux density from both flares. This aligns well with the ∼300 s duration of the enhancement.

We use the gamma-ray fluences of our GRBs to generate radio flux density predictions. Following V. V. Usov & J. I. Katz (2000) (also used in R. L. C. Starling et al. 2020), we take $\delta \sim 0.1\epsilon_B$ and $\beta \sim 1.6$. If we follow J. I. Katz (1997) and take $\epsilon_B = 10^{-3}$, using equation (3), we obtain 144 MHz flux density predictions of 32.0 and 76.3 mJy for the first and second flare, respectively. While the prediction for the first flare would remain hidden within the noise of the data, the second should be observable, and certainly, the combined radio flare should be visible. However, this is overpredicting the enhancement observed in the radio light curve.

The duration and timing of the low-significance radio flare would be consistent with coming from the prompt pulses of GRB 200925B if it lies at $z = 1.8$. In the following section, we look at how lowering ϵ_B can better reproduce our observations.

5.6 Constraining the fraction of energy in the magnetic field

In line with previous prompt studies, our results favour a lower fraction of energy in the magnetic field. LOFAR has the sensitivity to probe to this level, while challenges still remain in constraining microphysical parameters, including ϵ_B.

Given the presence of pulses seen in the *Swift*-BAT light curve, the LOFAR trigger time, and a redshift, we can produce constraints on ϵ_B for both cases of GRB 200925B and for GRB 240414A by varying this parameter within the magnetic reconnection model prediction to match our observations.

If we consider the flux density enhancement in the low-frequency light curve of GRB 200925B to be real, we can produce radio flux predictions over a parameter space of ranging redshift, β and ϵ_B, shown in Fig. 7, by keeping the third parameter constant. The high-frequency radio tail spectral index is kept constant at $\beta = 1.6$, following R. L. C. Starling et al. (2020, and references therein). Redshift is kept constant at $z = 1.8$, inferred from the delay between gamma-ray peak time and the start of the radio enhancement, testing the case in which the small flux density rise is a real radio flare. We can look for the parameter set that produces a radio flux density prediction equal to the enhancement seen in the radio light curve – any real radio emission emitted coincident with the gamma-ray pulse

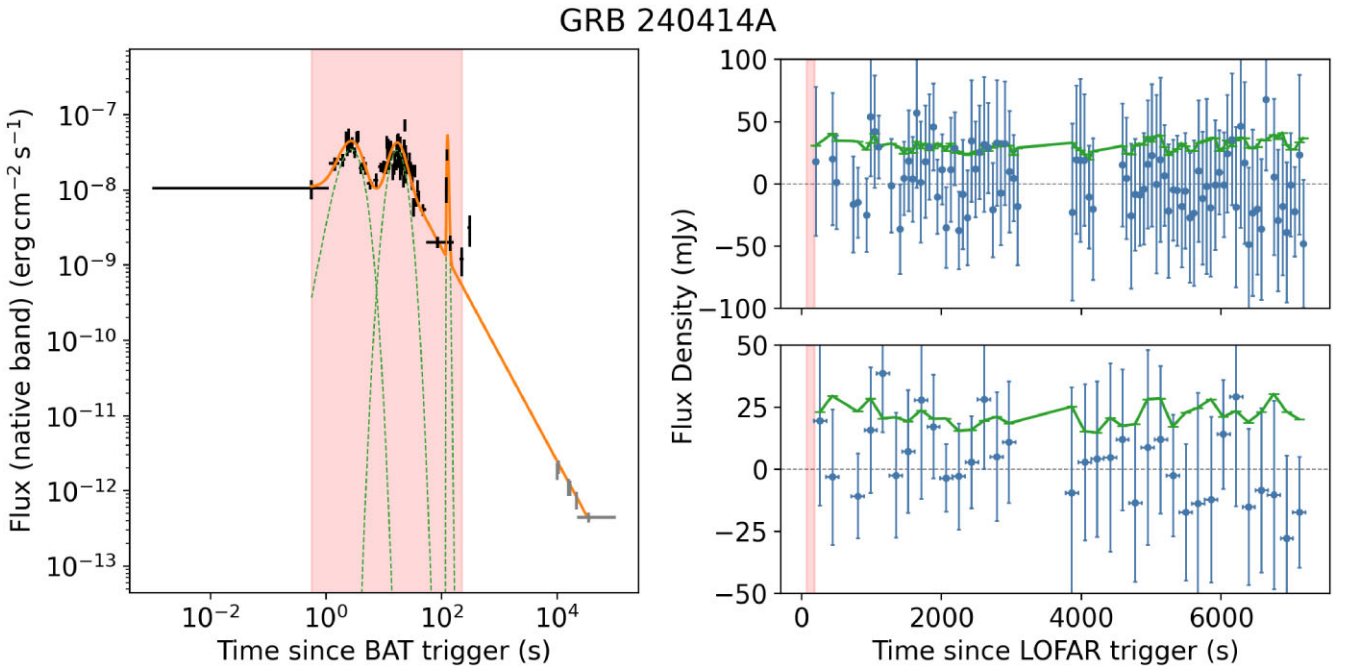

Figure 5. Left: The flux light curve of GRB 240414A for early BAT data (15–50 keV) and later XRT data (0.3–10 keV). Overlaid is the result of the GRB modelling described in Section 5 (and further details in A. Hennessy et al. 2023) – flare (dashed line) components are shown as well as total model fit (solid line). One power-law break and three flares are found for this burst. Right: The observed 144 MHz radio flux density at the position of GRB 240414A as a function of time. The top panel shows the 60 s time-sliced images, and the bottom panel shows the 180 s time-sliced images. The rms noise in each image is shown in green. The shaded region in all panels shows the predicted timing and duration of a radio flare corresponding to the reported redshift of 1.833. Some data points are missing due to poor-quality data.

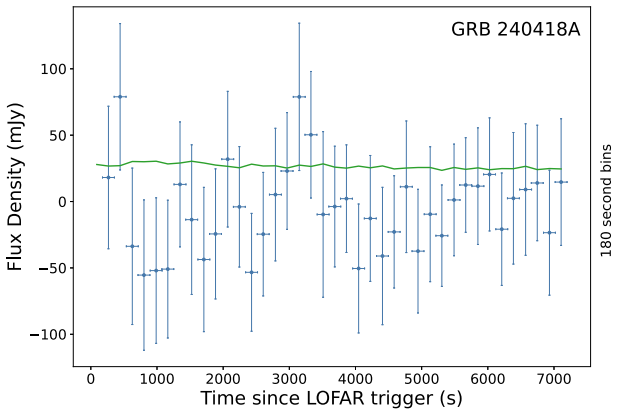

Figure 6. The observed 144 MHz flux density at the position of GRB 240418A as a function of time for 180 s time slices. The solid line shows the 1σ rms noise measured in each image.

should be equal to this observed level, or less, which represents a radio flare hidden within the noise of the data. Any greater flux density prediction should be seen in the data; hence, we can use this to produce upper limits on parameters. The white line represents this target flux density value, while the colour scale represents how far off this value other parameter sets predict. The GRB target position in the images across the enhancement has an average value of 34.7 mJy. At a value of $\epsilon_B = 4.2 \times 10^{-4}$, we satisfy the conditions to produce this observed flux density of two overlapping flares, emitted analogous to the two prompt pulses seen in the BAT data, for a redshift of 1.8. In the case of a complete non-detection, we can use our 3σ upper limit of 51.3 mJy from the rms noise of our 60 s time-sliced imaging to give an upper limit of $\epsilon_B < 5.6 \times 10^{-4}$ on any coherent radio flare activity at the 3σ significance level at $z = 1.8$. We note that there is uncertainty in our redshift value due to a lack of a reported redshift, spectroscopic or otherwise, though this value sits reasonably in the distribution of range of *Swift* GRB redshifts (P. A. Evans et al. 2009; G.-X. Lan et al. 2021).

For GRB 240414A, the quality of the data means the GRB position is not sampled across all the images, in particular some images during the expected arrival time of radio emission. Instead, we take the conservative 92.2 mJy 3σ rms value as the upper limit on any radio flare emission. As before, we plot the parameter space in Fig. 8. For redshift against ϵ_B, we keep $\beta = 1.6$ as a constant (following R. L. C. Starling et al. 2020). For β against ϵ_B, we keep redshift constant at 1.833, as reported in GCNs following this burst (C. Adami et al. 2024; A. Ugarte Postigo et al. 2024). We find an upper limit ϵ_B value of 2.76×10^{-4} to match our observations.

We discuss these limits in the context of our LOFAR campaign, and other literature, in Section 6.1.

5.7 Limitations

Across this study, we have adopted a value of DM $\sim 1200z$ following D. R. Lorimer et al. (2007). J. P. Macquart et al. (2020) and C. W. James et al. (2022) discuss the assumptions and limitations of this relation in further detail. Additionally, the populations of FRBs (fast radio bursts), a different type of astrophysical transient, on which these DM measures are based may not reflect the local GRB environment. LGRBs preferentially occur in galaxies with high star formation rates (S. Savaglio, K. Glazebrook & D. Le Borgne 2009), meaning we may expect denser environments around the progenitor. Below a redshift $z \lesssim 2$, we may expect the contribution to dispersion

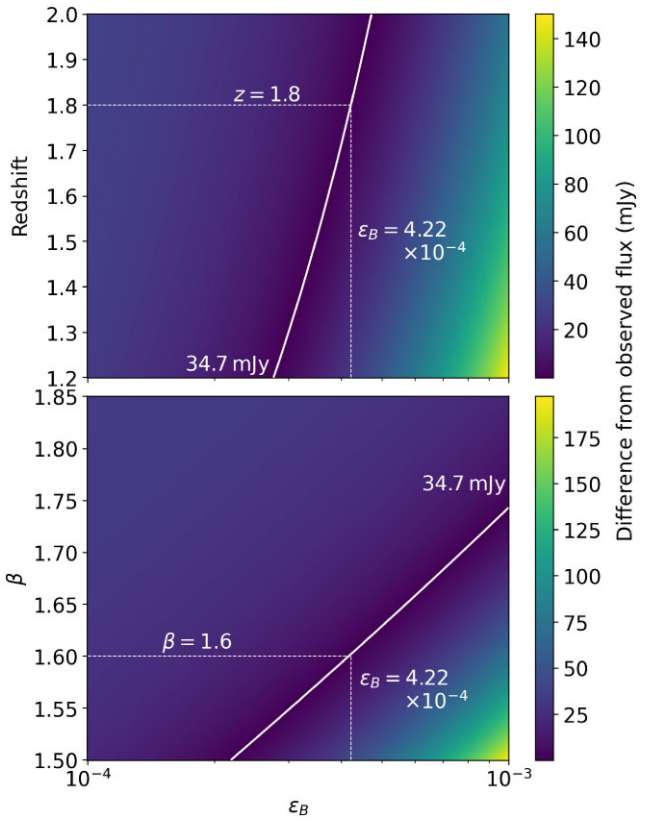

Figure 7. The parameter space for ϵ_B against redshift for constant $\beta = 1.6$ (top) and ϵ_B against β for constant $z = 1.8$ (bottom) for GRB 200925B. The solid line represents the parameter set that produces the 'target' value of 34.7 mJy, obtained as the average flux density across the small bump in the radio light curve. The dashed line represents the redshift that provides the correct timing constraint for this bump, and correspondingly, the required ϵ_B given this value. The scale represents how far off from the target value that parameter set produces.

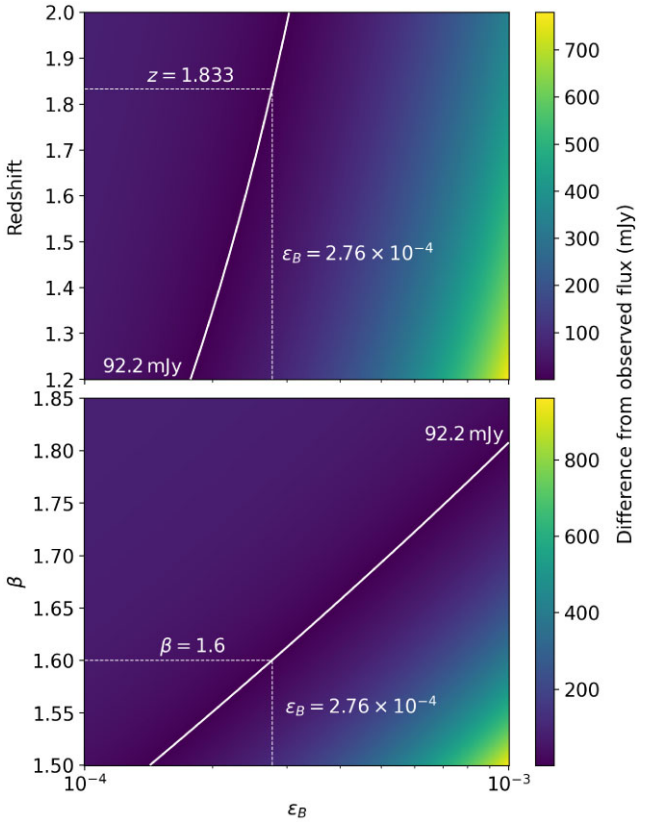

Figure 8. The parameter space for ϵ_B against redshift for constant $\beta = 1.6$ (top) and ϵ_B against β for constant $z = 1.833$ (bottom) for GRB 240414A. The solid line represents the parameter set that produces the 'target' value of 92.2 mJy, obtained as 3σ image rms across the radio light curve. The dashed line represents the redshift that provides the correct timing constraint for this bump, and correspondingly, the required ϵ_B given this value. The scale represents how far off from the target value that parameter set produces.

due to molecular clouds within the host galaxy to become important. A higher DM on one hand favours our observations, as the delay $\tau(\nu)$ of radio emissions is proportional to DM, resulting in the later arrival of radio flares and relaxing the time required for a radio observatory to get on target. On the other hand, the expected flux density of radio emission is inversely proportional to DM and so any emission becomes even fainter.

The results and interpretation here also assume that other propagation effects are not heavily impacting our observations. Radio emission could be self-absorbed locally, or the plasma comoving frequency may be sufficiently high that some radio emission is cut off. These would act to reduce the radio flux reaching the observer, meaning we are overpredicting what we are expecting to see – instead any incoming signals may be lost within the noise of the data, if any escapes the progenitor region at all. Although we cannot quantify these effects, previous works have suggested that they can be very small (B. Zhang 2014) – see A. Rowlinson & G. E. Anderson (2019) for an in-depth discussion of low-frequency radio emission and the propagation effects that may occur.

One key limitation in being able to more robustly constrain ϵ_B in the context of our magnetic wind model is the lack of a spectroscopic redshift in many bursts. When a redshift is available, we can predict the timing of radio flares and use flux density measurements across this time period to place constraints on our model, rather than using the rms across the whole observation.

6 DISCUSSION

We have carried out a rapid follow-up search for 144 MHz coherent radio emission in four LGRBs, finding no evidence of significant emission in any case. In the following sections, we discuss these results in the context of our full LOFAR rapid follow-up campaign, previous literature estimates of the ϵ_B parameter, and future prospects of prompt radio follow-up of GRBs.

6.1 LOFAR rapid follow-up campaign

Our LOFAR campaign has followed up six *Swift* LGRBs and one SGRB over a period of 6 yr, during which the trigger criteria have evolved. This collection of GRBs does not therefore form a sample in a statistical sense and are analysed here individually, but acts as a pilot for future more homogeneously selected events. The LGRBs within this sample are summarized in Table 3. We find that the bursts in this sample are all 'standard' in our usual expectations for LGRBs. Temporally, they look to have some or all of the components of a canonical light curve. In the distribution of isotropic energy, luminosity, and redshift parameters among the population of *Swift* GRBs, they look average (S.-X. Yi et al. 2016). They also sit

Table 3. Summary of the sample of LGRBs observed as part of the LOFAR rapid response follow-up campaign. The search for radio emission in GRB 180706A was investigated through a magnetar central engine model, as opposed to looking for emission analogous to prompt gamma-ray pulses or X-ray flares.

GRB	BAT T90 (s)	z	LOFAR $T_{\rm start}$ (s since BAT trigger)	S_ν limit (2 h) (mJy)	3σ S_ν time-sliced limits Bin length (s)	Limit (mJy)	ϵ_B constraint	References
180706A	42.7 ± 8.7	≤ 2	260	1.7 beam^{-1}	30	28 beam^{-1}	$\lesssim$[0.24–0.47]	[1], [2]
					120	11 beam^{-1}		
200925B	18.25 ± 0.97	~ 1.8	267	3.1	60	51.3	$<4.22 \times 10^{-4}$	This work, [3]
					180	28.8		
210104A	32.06 ± 0.49	0.46	269	3.6	60	73.5	–	This work, [4], [5]
					180	45.3		
210112A	107.6 ± 13.0	~ 2	511	3	60	87.0	$\lesssim 10^{-4}$	[6], [7], [8]
					320	42.0		
240414A	88.28 ± 50.41	1.833	373	3.1	60	92.2	$<2.76 \times 10^{-4}$	This work, [9], [10]
					180	65.4		
240418A	12.00 ± 3.61	–	373	4.8	60	157.0	–	This work, [11]
					180	79.5		

Note. References: [1] A. Rowlinson et al. (2019), [2] T. Sakamoto et al. (2018), [3] M. Stamatikos et al. (2020), [4] D. M. Palmer et al. (2021), [5] L.-L. Zhang et al. (2022), [6] A. Hennessy et al. (2023), [7] M. Stamatikos et al. (2021), [8] D. A. Kann et al. (2021), [9] C. B. Markwardt et al. (2024), [10] C. Adami et al. (2024), and [11] D. M. Palmer et al. (2024).

comfortably on the Amati relation for LGRBs (L. Amati 2006), a correlation between the peak energy of the prompt burst spectrum and the intrinsic isotropic energy of the burst; and the spectral hardness–T90 distribution among *Swift* bursts (C. Kouveliotou et al. 1993; A. Lien et al. 2016) showing we are not probing any particularly outlying parameter space.

A previous study searched for low-frequency emission in GRB 210112A (A. Hennessy et al. 2023) for which a tentative redshift estimate was available, rather than an accurate spectroscopic measurement. In this study, we include two GRBs for which spectroscopically derived redshifts have been reported: GRB 210104A and GRB 240414A, which allow us to exactly identify the time window that low-frequency pulses are predicted to occur in, and directly probe coherent radio emission related to the energetic processes in the prompt phase. GRB 240414A has both a robust redshift and clear flaring activity; however, the LOFAR observing window catches only the end of the flaring period. GRB 210104A and GRB 240418A presented in this paper are blindly searched for any persistent or flaring radio activity, in the former case due to prompt radio activity not being within the observation window, and in the latter due to a lack of redshift and any gamma/X-ray flaring in the *Swift* light curve. GRB 200925B had no reported redshift and also constitutes a blind search, which recovers a marginal flux density enhancement, discussed in Section 5.5.

We did not detect significant signs of radio emission in any case, but this may not be unexpected: the results of this paper are in line with our previous study of GRB 210112A (A. Hennessy et al. 2023), where we commonly conclude that a lower value of ϵ_B is likely required, where the model consequently produces radio predictions at or lower than typical noise levels within LOFAR images. For the initial model input of $\epsilon_B = 10^{-3}$, LOFAR is expected to be more than sensitive enough to have observed most of the predicted radio flares.

An alternative means of producing coherent radio emission is through a rapidly rotating, magnetized neutron star (A. Rowlinson et al. 2019). Even if only formed for a short duration, this provides a method of producing persistent or pulsed radio emission. As the remnant spins down, emission can occur through dipole magnetic breaking (T. Totani 2013). Some models predict the formation of such objects during a GRB (A. Rowlinson et al. 2010, 2013). X-ray plateaus seen in some afterglows are a feature associated with these objects (B. Zhang & P. Mészáros 2001; B. Zhang 2014). See A. Rowlinson & G. E. Anderson (2019, and references therein) for a further discussion of the magnetar model. We do not consider this model in this paper, but previous studies have looked for such emission (e.g. A. P. Curtin et al. 2023), including two bursts followed up by LOFAR. The first LGRB of the LOFAR campaign, GRB 180706A, was interpreted in this framework of magnetar models. While flares were present in the early *Swift* data, they did not fall in LOFAR's observation window, and so this burst could not be probed for low-frequency emission through the magnetic wind model. Instead, the plateau phase is probed, looking for evidence of a magnetar forming and producing persistent or flaring radio activity. No short-duration emission is found to deep limits, though this does not rule out the model. More notably, a candidate radio flash was detected and shown to be associated with the short GRB 201006A (A. Rowlinson et al. 2024). This is shown to be consistent with emission from prolonged central engine activity through the formation of a magnetar during the burst. This was a burst followed up by LOFAR in rapid response mode, but not included here as it is a short-duration GRB expected to have been formed from a compact binary merger, rather than stellar collapse.

6.2 Previous estimates of ϵ_B

The implications for ϵ_B generated in our study are also in agreement with other recent literature publishing constraints on this parameter, derived through a variety of methods and at a variety of times. This is visualized in Fig. 9 where we show our constraints from our LOFAR sample alongside other literature. These studies look at different phases within the GRB; we may expect varying ϵ_B values as the prompt and afterglow do not necessarily reflect the same mechanisms. The variety of values and their large uncertainties highlight the challenge in understanding the contribution of a magnetic field in a GRB jet.

R. Santana, R. Barniol Duran & P. Kumar (2014) study the forward shocks of GRBs to obtain ϵ_B values using both an X-ray and an optical sample. By assuming the end of the steep decay phase in *Swift* light curves is the decaying forward shock, they deduce upper limits of $10^{-8} \lesssim \epsilon_B \lesssim 10^{-3}$. By assuming the observed optical flux arises due to the forward shock, they derive limits of $10^{-6} \lesssim \epsilon_B \lesssim 10^{-3}$, with medians of $\sim 10^{-5}$ for both X-ray and optical derived limits.

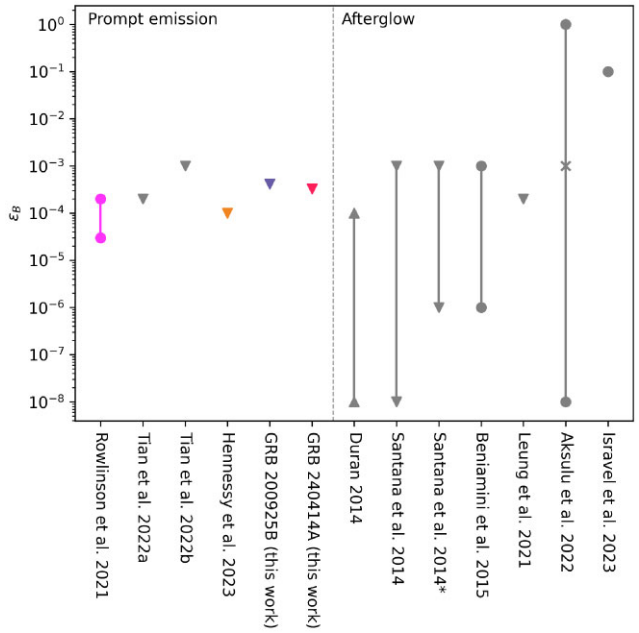

Figure 9. ϵ_B estimates from prompt emission (left of dashed line) and afterglow modelling (right of dashed line) presented from recent literature and this LOFAR sample, sorted in order of publishing year. Up caret are lower limit values, down caret are upper limit values, and circles are measured values.

Alternatively, some studies look at afterglows as a means of constraining the structure of the GRB jet and its surrounding environment. In a systematic study of magnetic fields in forward shocks, R. Barniol Duran (2014) used the time and flux of the GRB radio afterglow peak to determine ϵ_B, assuming the radio emission is produced by the external forward shock. They find limits ranging $\sim 10^{-8}$–10^{-4}, with a median at $\sim 10^{-5}$. Using Bayesian inference, M. D. Aksulu et al. (2022) study a sample of long- and short-GRB afterglow data sets to infer the parameters of the outflow. They find a wide range of values $10^{-8} \lesssim \epsilon_B \lesssim 1$, with an average of $\sim 10^{-3}$. J. K. Leung et al. (2021) studied the late radio afterglow of GRB 171205A and, in combination with early-time radio observations, showed the progenitor could have originated in a stellar wind medium through the evolution of the radio spectral energy distribution – through this, estimating shock parameters of the burst, including an estimate of $\epsilon_B = 2 \times 10^{-4}$. P. Beniamini et al. (2015) used GeV and X-ray fluxes to estimate ϵ_B, assuming that the electrons are fast cooling and that the X-ray flux is not suppressed by synchrotron self-Compton (SSC) absorption, determining weak magnetic fields and $10^{-6} \lesssim \epsilon_B \lesssim 10^{-3}$. In a study of the emission of GRB 221009A, a hybrid model is used, where synchrotron radiation explains optical to X-ray emissions and a proton-synchrotron process explains the very high energy afterglow – this model requires a significant fraction of energy in the magnetic field $\epsilon_B \sim 0.1$ (H. Isravel, D. Bégué & A. Pe'er 2023). This is possibly a more unique case where the presence of a highly magnetized environment, for example within a supernova remnant, allows for the presence of TeV emission otherwise suppressed by SSC.

With improvements to radio facilities' response times and sensitivities, some recent studies alongside our LOFAR sample have looked to probe for prompt radio emission. A. Rowlinson et al. (2021) place a constraint of $3 \times 10^{-5} \lesssim \epsilon_B \lesssim 2 \times 10^{-4}$ with a LOFAR follow-up of short GRB 181123B, looking for radio emission predicted to occur in the collapse of a neutron star into a black hole. J. Tian et al. (2022a) determine a constraint of $\epsilon_B \lesssim 2 \times 10^{-4}$ in a very rapid follow-up study of short GRBs, based on a non-detection and limiting sensitivity of MWA with an assumed formation of a magnetar. And in an MWA rapid follow-up of GRB 210419A, J. Tian et al. (2022b) look for radio emission on minute time-scales, finding no detection but placing upper limits of radio emission analogous to X-ray flaring activity resulting in an upper limit of $\epsilon_B \lesssim 10^{-3}$.

6.3 Future prospects

The typical LOFAR rapid response of ∼5 min in this campaign currently allows us to access gamma-ray pulses or X-ray flares for $z > 1$. With the upgrade to LOFAR 2.0,[8] we should expect a much faster trigger response time and many more triggers. A response time of 1 min means that we should expect to observe, accounting for a dispersion delay, all significant radio emission starting from the BAT trigger time for $z > 0.25$. Given that many gamma-ray pulses and X-ray flares will occur in the first few tens of seconds, if not later, this condition is relaxed further. With such a rapid response time, the vast majority of predicted radio flares become observable.

With the prompt gamma-ray emission accessible to LOFAR 2.0, we can determine the expected detection rate of radio pulses directly from gamma-ray pulses, following the method described in R. L. C. Starling et al. (2020). Based on the common conclusions across our LOFAR campaign and magnetic wind model, we calculate these flux density predictions using $\epsilon_B = 4 \times 10^{-4}$. The sensitivity limit is calculated using equation (5) in R. L. C. Starling et al. (2020), extrapolated from the baseline sensitivity of 1 mJy for a 2 h observation with LOFAR 2.0. We obtained the entire catalogue of *Swift*-BAT GRB prompt emission light curves with redshift from the GRB products available at the UKSSDC,[9] and fitted them using a version of the code, described in A. Hennessy et al. (2023), specifically for BAT prompt emission data. From the output of 1325 individual fitted pulses across this sample, we determine that 55 per cent of pulses are bright enough to be observable to LOFAR 2.0 for this lower ϵ_B, this is shown by the population of pulses above the red sensitivity line in Fig. 10. We also estimate the lower limit of ϵ_B that we can probe, assuming all other assumptions hold in this model, finding the detected fraction drops to 1 per cent for $\epsilon_B \sim 5.3 \times 10^{-6}$. Some studies suggest that ϵ_B may be as low as 10^{-8} for some bursts. For such a low value, the resultant radio emission in this framework is below the sensitivity of even LOFAR 2.0. If these values are common, this introduces significant uncertainty into the predicted detection rates. Ranges for ϵ_B going down to as low as 10^{-8} have been estimated for the afterglow phase, while the prompt phase estimates to date, relevant to rapid radio follow-up, remain above 3×10^{-5} (A. Rowlinson et al. 2021).

This promises that current generation radio facilities offer an opportunity to further constrain GRB jets and their environments, utilizing the earlier and brighter pulses. A larger set of triggers will allow us to more confidently place constraints on radio emission emitted analogous to prompt emission pulses, especially with a growing number of bursts with redshifts.

The *Space Variable Objects Monitor* (*SVOM*; J. L. Atteia, B. Cordier & J. Wei 2022) mission has launched in 2024. It can provide GRB triggering in the soft X-ray regime at 4 keV, lower than other currently operating missions. This means early access to this regime than *Swift*-XRT can typically provide. Similarly, the *Einstein Probe*

[8] https://www.lofar.eu/wp-content/uploads/2023/04/LOFAR2_0_White_Paper_v2023.1.pdf
[9] https://www.swift.ac.uk/xrt_products/

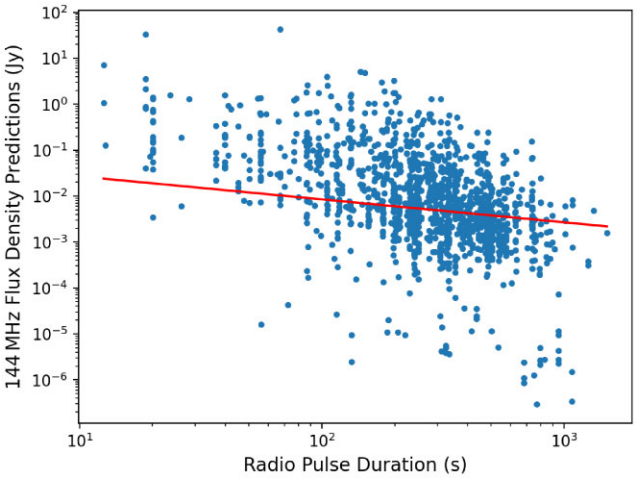

Figure 10. Predictions for the radio flux density for all *Swift*-BAT pulses with redshift. Above the line indicates pulses which are detected based on the expected sensitivity and faster response of LOFAR 2.0, and a lower $\epsilon_B = 4 \times 10^{-4}$ in line with the conclusions of our LOFAR sample study. A 55 per cent detection fraction is expected in this framework for BAT pulses.

(*EP*) mission (W. Yuan et al. 2022) provides a wide-field triggering XRT, operating at 0.5–4 keV.

The SKA-Low (Square Kilometre Array Low Frequency Telescope; P. E. Dewdney et al. 2009) represents the next generation of radio telescope. It will operate in the 50–300 MHz frequency range and offer deeper sensitivity than current telescopes like LOFAR and MWA. For 60 and 180 s integration times like the images created in this study, we can expect sensitivities[10] on the order of a few 0.1 mJy (M. Sokolowski et al. 2022). Compared to the limits of a few tens of mJy in this paper, this is an improvement of two orders of magnitude.

To further probe the mechanics of the GRB inner engine, and the predictions of radio emission analogous to gamma-ray and X-ray flares, we need continued rapid follow-up observations of GRB with radio facilities like LOFAR and MWA, alongside continued *Swift*, *SVOM*, *EP*, and other high-energy GRB triggering facilities. A large sample of bursts is important especially due to the unpredictability of GRB pulses/flares (if any occur at all), uncertainty within the model parameters, and limited knowledge of the environment and its effects on emission – immediately around the burst, and in host galaxies. A large sample provides the ability to fold sample parameter distributions through observed flux limit distributions, to give better statistics. In addition, optical follow-up to provide consistent and accurate spectroscopic redshifts will allow us to probe the model with more confidence.

7 CONCLUSION

In this paper, we have presented the *Swift* and LOFAR HBA rapid-response observations of four LGRBs. For two of them, we directly test a magnetic wind model, predicting and looking for radio emission emitted analogous to the observed pulses seen at gamma-ray and X-ray wavelengths. A detection in line with predictions would evidence the GRB jet is Poynting flux dominated.

No significant emission is detected in any of the observations, at either 60 or 180 s time-scales. Assuming the V. V. Usov & J. I. Katz (2000) magnetic wind model, our constraints suggest the input parameters must be tweaked to account for the measured flux density limits, which are typically low. Primarily, a key unknown is the proportion of internal energy in the magnetic fields behind the shock – our radio predictions are heavily dependent on this value, and based on a non-detection, we were able to derive limits on this parameter for GRBs emitting prompt radio emission alongside other more energetic wavelengths.

In GRB 200925B, we produce 3σ 144 MHz flux density upper limits of 51.3 and 28.8 mJy for 60 and 180 s time slices, respectively. We see a small rise in flux with a low significance of 2σ. If it were real, it falls in line with timing and duration predictions for $z = 1.8$ and would imply an ϵ_B upper limit of 4.2×10^{-4} to match our observations. If it were not real, we produce an upper limit of 5.6×10^{-4}. In GRB 240414A, based on 180 s 3σ 144 MHz flux density upper limit of 92.2 mJy, we produce an ϵ_B upper limit of 2.8×10^{-4}. In 60 s time slices, we find a radio upper limit of 65.4 mJy. For the remaining two bursts, we could not directly test radio emission from prompt engine activity, but we produced similar 60 and 180 s observed flux density limits of 73.5 and 45.3 mJy for GRB 210104A, and 157 and 79.5 mJy for GRB 240418A.

The weak redshift constraints for some GRBs present a further challenge in constraining the model. Given a redshift for GRB 200925B, we would be able to more concretely accept or rule out the possibility of the small flux density enhancement, and in general, a precise redshift means our predictions can be more certain both in terms of timing and energetics of incoming prompt radio emission.

With the advent of new and enhanced facilities for both triggering and follow-up, we will be able to build samples with the capability to more robustly test magnetically dominated models of GRB jets.

ACKNOWLEDGEMENTS

The authors would like to thank the anonymous reviewer for their valuable feedback, which has greatly improved this work. AH was supported by an UK Science and Technology Facilities Council (STFC) Studentship. RLCS was supported by a Leverhulme Trust Research Project grant RPG-2023-240 and acknowledged the ASTRON/JIVE Helena Kluyver visitor programme, which supported the early phases of this work. AR and IdR acknowledge funding from the Nationale Wetenschapsagenda (NWA) CORTEX grant (NWA.1160.18.316) of the research programme NWA-ORC (Onderzoek op Routes door Consortia), which is (partly) financed by the Dutch Research Council (NWO). NRT acknowledges support through STFC consolidated grant ST/W000857/1. This research used the ALICE High Performance Computing facility at the University of Leicester. This work made use of data supplied by the UK Swift Science Data Centre at the University of Leicester. This paper is based (in part) on data obtained with the LOFAR telescope (LOFAR-ERIC) under project codes LC10_012 (PI: Rowlinson), LC14_004 (PI: Starling), LC15_013 (PI: Starling), and LC20_021 (PI: Rowlinson). LOFAR (M. P. Haarlem et al. 2013) is the Low Frequency Array designed and constructed by ASTRON. It has observing, data processing, and data storage facilities in several countries, which are owned by various parties (each with their own funding sources), and which are collectively operated by the LOFAR European Research Infrastructure Consortium (LOFAR-ERIC) under a joint scientific policy. The LOFAR-ERIC resources have benefited from the following recent major funding sources: CNRS-INSU, Observatoire de Paris and Université d'Orléans, France; BMBF, MIWF-NRW, MPG, Germany; Science Foundation Ireland (SFI), Department of Business, Enterprise and Innovation (DBEI), Ireland; NWO, The

[10] https://sensitivity-calculator.skao.int/low

Netherlands; The Science and Technology Facilities Council, UK; and Ministry of Science and Higher Education, Poland. For the purpose of open access, the author has applied a Creative Commons Attribution (CC BY) licence to the Author Accepted Manuscript version arising from this submission.

DATA AVAILABILITY

LOFAR data underlying the findings are openly available in the LOFAR Long-Term Archive (LTA) accessible via https://lta.lofar.eu. *Swift* data and XRT products are openly available via the UK *Swift* Science Data Centre (UKSSDC) at www.swift.ac.uk.

REFERENCES

Adami C., Ilbert O., de la Torre S., de Ugarte Postigo A., Schneider B., Le Floc'h E., 2024, GCN Circ., 36085, 1
Aksulu M. D., Wijers R. A. M. J., van Eerten H. J., van der Horst A. J., 2022, MNRAS, 511, 2848
Amati L., 2006, MNRAS, 372, 233
Anderson G. E. et al., 2018, MNRAS, 473, 1512
Anderson G. E. et al., 2021, Publ. Astron. Soc. Aust., 38, e026
Atteia J. L., Cordier B., Wei J., 2022, Int. J. Mod. Phys. D, 31, 2230008
Barniol Duran R., 2014, MNRAS, 442, 3147
Barthelmy S. D. et al., 2005, Space Sci. Rev., 120, 143
Beniamini P., Granot J., 2016, MNRAS, 459, 3635
Beniamini P., Nava L., Duran R. B., Piran T., 2015, MNRAS, 454, 1073
Burrows D. N. et al., 2005, Space Sci. Rev., 120, 165
Cepa J., 1998, Ap&SS, 263, 369
Chandra P., Frail D. A., 2012, ApJ, 746, 156
Curtin A. P. et al., 2023, ApJ, 954, 154
de Gasperin F. et al., 2019, A&A, 622, A5
de Ugarte Postigo A., Kann D. A., Thoene C. C., Blazek M., Agui Fernandez J. F., Aceituno F., 2020, GCN Circ., 28501, 1
de Ugarte Postigo A. et al., 2024, GCN Circ., 36087, 1
Dewdney P. E., Hall P. J., Schilizzi R. T., Lazio T. J. L. W., 2009, Proc. IEEE, 97, 1482
Dichiara S. et al., 2024, GCN Circ., 36104, 1
Evans P. A. et al., 2007, A&A, 469, 379
Evans P. A. et al., 2009, MNRAS, 397, 1177
Evans P. A. et al., 2010, A&A, 519, A102
Gehrels N. et al., 2004, ApJ, 611, 1005
Granot J., van der Horst A. J., 2014, Publ. Astron. Soc. Aust., 31, e008
Hancock P. J. et al., 2019, Publ. Astron. Soc. Aust., 36, e046
Hennessy A. et al., 2023, MNRAS, 526, 106
Intema H. T., Jagannathan P., Mooley K. P., Frail D. A., 2017, A&A, 598, A78
Isravel H., Bégué D., Pe'er A., 2023, ApJ, 956, 12
James C. W., Prochaska J. X., Macquart J.-P., North-Hickey F. O., Bannister K. W., Dunning A., 2022, MNRAS, 509, 4775
Kann D. A. et al., 2011, ApJ, 734, 96
Kann D. A., de Ugarte Postigo A., Thoene C. C., Blazek M., Agui Fernandez J. F., Sota A., 2021, GCN Circ., 29296, 1
Karambelkar V. et al., 2024, GCN Circ., 36199, 1
Katz J. I., 1997, ApJ, 490, 633
Kennea J. A. et al., 2021, GCN Circ., 29260, 1
Klebesadel R. W., Strong I. B., Olson R. A., 1973, ApJ, 182, L85
Kosogorov N. et al., 2025, ApJ, 985, 265
Kouveliotou C., Meegan C. A., Fishman G. J., Bhat N. P., Briggs M. S., Koshut T. M., Paciesas W. S., Pendleton G. N., 1993, ApJ, 413, L101
Kumar P., Zhang B., 2015, Phys. Rep., 561, 1
Lan G.-X., Wei J.-J., Zeng H.-D., Li Y., Wu X.-F., 2021, MNRAS, 508, 52
Lazzati D., Morsony B. J., Margutti R., Begelman M. C., 2013, ApJ, 765, 103
Leung J. K. et al., 2021, MNRAS, 503, 1847
Lien A. et al., 2016, ApJ, 829, 7
Lorimer D. R., Bailes M., McLaughlin M. A., Narkevic D. J., Crawford F., 2007, Science, 318, 777
Ma G.-L., Xie W., Wang W.-K., Dong A.-J., Zhi Q.-J., 2024, Astron. Nachr., 345, e20230179
Macquart J. P. et al., 2020, Nature, 581, 391
Markwardt C. B. et al., 2024, GCN Circ., 36140, 1
Norris J. P., Nemiroff R. J., Bonnell J. T., Scargle J. D., Kouveliotou C., Paciesas W. S., Meegan C. A., Fishman G. J., 1996, ApJ, 459, 393
Offringa A. R., de Bruyn A. G., Biehl M., Zaroubi S., Bernardi G., Pandey V. N., 2010, MNRAS, 405, 155
Offringa A. R., van de Gronde J. J., Roerdink J. B. T. M., 2012, A&A, 539, A95
Offringa A. R. et al., 2014, MNRAS, 444, 606
Palmer D. M. et al., 2021, GCN Circ., 29251, 1
Palmer D. M. et al., 2024, GCN Circ., 36254, 1
Pe'er A., Mészáros P., Rees M. J., 2007, Philos. Trans. R. Soc. A, 365, 1171
Rees M. J., Meszaros P., 1994, ApJ, 430, L93
Rhodes L. et al., 2024, MNRAS, 533, 4435
Ror A. K., Gupta R., Aryan A., Pandey S. B., Oates S. R., Castro-Tirado A. J., Kumar S., 2024, ApJ, 971, 163
Rowlinson A., Anderson G. E., 2019, MNRAS, 489, 3316
Rowlinson A. et al., 2010, MNRAS, 409, 531
Rowlinson A., O'Brien P. T., Metzger B. D., Tanvir N. R., Levan A. J., 2013, MNRAS, 430, 1061
Rowlinson A. et al., 2019, MNRAS, 490, 3483
Rowlinson A. et al., 2021, MNRAS, 506, 5268
Rowlinson A. et al., 2024, MNRAS, 534, 2592
Ryde F. et al., 2010, ApJ, 709, L172
Sakamoto T. et al., 2018, GCN Circ., 22921, 1
Santana R., Barniol Duran R., Kumar P., 2014, ApJ, 785, 29
Sari R., Piran T., 1997, MNRAS, 287, 110
Savaglio S., Glazebrook K., Le Borgne D., 2009, ApJ, 691, 182
Sbarufatti B. et al., 2020, GCN Circ., 28508, 1
Schmitt J. et al., 2024, A&A, 687, A198
Smolsky M. V., Usov V. V., 2000, ApJ, 531, 764
Sokolowski M. et al., 2022, Publ. Astron. Soc. Aust., 39, e015
Staley T. D., 2014, Astrophysics Source Code Library, record ascl:1411.003
Stamatikos M. et al., 2020, GCN Circ., 28506, 1
Stamatikos M. et al., 2021, GCN Circ., 29297, 1
Starling R. L. C., Rowlinson A., van der Horst A. J., Wijers R. A. M. J., 2020, MNRAS, 494, 5787
Swinbank J. D. et al., 2015, Astron. Comput., 11, 25
Taylor J. H., Cordes J. M., 1993, ApJ, 411, 674
Tian J. et al., 2022a, Publ. Astron. Soc. Aust., 39, e003
Tian J. et al., 2022b, MNRAS, 514, 2756
Tingay S. J. et al., 2013, Publ. Astron. Soc. Aust., 30, e007
Tohuvavohu A. et al., 2024, GCN Circ., 36181, 1
Totani T., 2013, PASJ, 65, L12
Usov V. V., 1992, Nature, 357, 472
Usov V. V., Katz J. I., 2000, A&A, 364, 655
van der Horst A. J. et al., 2008, A&A, 480, 35
van Haarlem M. P. et al., 2013, A&A, 556, A2
van Weeren R. J. et al., 2016, ApJS, 223, 2
Waxman E., Kulkarni S. R., Frail D. A., 1998, ApJ, 497, 288
Williams W. L. et al., 2016, MNRAS, 460, 2385
Yi S.-X., Xi S.-Q., Yu H., Wang F. Y., Mu H.-J., Lü L.-Z., Liang E.-W., 2016, ApJS, 224, 20
Yuan W., Zhang C., Chen Y., Ling Z., 2022, in Bambi C., Santangelo A., eds, Handbook of X-ray and Gamma-ray Astrophysics. Springer, Singapore, p. 1
Zhang B., 2014, ApJ, 780, L21
Zhang B., Mészáros P., 2001, ApJ, 552, L35
Zhang L.-L. et al., 2022, ApJ, 941, 63

This paper has been typeset from a TEX/LATEX file prepared by the author.